Journal of Sound and Vibration 607 (2025) 119030

Contents lists available at ScienceDirect

Journal of Sound and Vibration

journal homepage: www.elsevier.com/locate/jsvi

An extended semi-analytical finite element method for modeling guided waves in plates with pillared metasurfaces

S. Mariani *, A. Palermo, A. Marzani

Department of Civil, Chemical, Environmental and Materials Engineering — DICAM, University of Bologna, Viale del Risorgimento 2, Bologna, 40136, Italy

ARTICLE INFO

Keywords:
Metamaterials
Metaplates
Resonator
SAFE
Lamb
Scholte

ABSTRACT

This work presents a semi-analytical finite element (SAFE) scheme for modeling guided waves in plates equipped with arrays of resonators, known as metasurfaces. The method requires only the finite element discretization of the waveguide's cross-section, with the resonators' dynamic effects incorporated as a traction condition on the plate surface. Through this approach, the general SAFE framework is extended to account for a metasurface of linear resonators atop the plate, thereby broadening its applicability to metamaterial design. Dispersion properties, including wave propagation and attenuation, band gap information, and wave shapes, are obtained by solving a linearized eigenvalue problem. Furthermore, the method enables the computation of both frequency and time responses for a generic forcing function at an arbitrary source–receiver distance. A viscoelastic steel plate, either in vacuum or in water, coupled to an array of mass–spring–dashpot oscillators, is considered, and Lamb, quasi-Lamb, and quasi-Scholte modes, existing in the fluid-coupled scenario, are computed and discussed. The algorithm offers enormous computational advantages over other techniques established in the field of metamaterials. Consequently, it can greatly aid the development of pillared metaplates and potentially other engineered structures, as the method can be further generalized to address waveguides of arbitrary cross-sections and anisotropic media.

1. Introduction

The propagation of elastic waves in thin structural components such as plates is a fundamental area of research with wide-ranging applications in non-destructive evaluation (NDE) [1] and structural health monitoring (SHM) [2]. Dispersion curves [3], which describe the relationship between wave frequency and wavenumber, are essential for understanding the wave propagation phenomena, since they can offer insights into, e.g., phase velocities, attenuation, and modal shapes. Among the most popular approaches to compute dispersion curves are the Global Matrix Method [4,5], which solves a system of linear equations derived from wave equations and boundary conditions, and the wave finite element (WFE) method [6,7], which processes the stiffness and mass matrices of a waveguide segment using periodicity conditions. However, the former scheme often encounters numerical difficulties in obtaining all solutions of the dispersion relations, while the latter one is not well suited for the computation of transient signals propagating through the modeled waveguide in response to an external force. These difficulties can be overcome by utilizing semi-analytical finite element (SAFE) methods, which reduce the 3D wave analysis to a 1D (for plates) or 2D (for waveguides of arbitrary shapes) cross sectional problem by discretizing the structure cross section [8–11].

* Corresponding author.
E-mail address: stefano.mariani9@unibo.it (S. Mariani).

https://doi.org/10.1016/j.jsv.2025.119030
Received 3 January 2025; Received in revised form 20 February 2025; Accepted 23 February 2025
Available online 4 March 2025

In recent years, there has been a surge of interest around the dispersion properties of periodic structures, fueled by material scientists and physicists working on metamaterials. In the field of elastodynamics, metamaterials are artificially engineered structures designed to manipulate elastic wave propagation in order to achieve properties such as negative effective mass density or stiffness, bandgaps, and tailored dispersion characteristics that are not found in natural materials. An example of an elastic metamaterial is a plate decorated with an array of resonators on its surface, commonly referred to as a metasurface. This type of structure was first studied by Pennec et al. [12] and Wu et al. [13] in 2008. Both works showed that a band gap may appear in the dispersion curves, which depends on both a resonator's mode and a plate's mode involved in the coupling. The tunability of these systems, driven by parameters such as resonator mass, stiffness, and damping, makes them a focal point of recent research in wave physics and engineering. For example, several studies have focused on broadening the wave attenuation frequency spectrum of pillared plates by combining Bragg band gaps, induced by periodicity, with hybridization band gaps, driven by local resonances [12,14,15]. Besides vibration attenuation, wave steering, mode conversion and energy focusing have been demonstrated in pillared metasurfaces through the design of graded arrays, lenses and waveguides [16–19]. Recently, more complex dynamic phenomena such as topological waveguiding, unidirectional wave control and generation of bound states have been achieved by adopting dedicated pillar designs such as chiral [20] and time modulated resonators [21], or peculiar pillar arrangements such as quasi-periodic [22], clustered [23] or ring-like arrays [24]. The recent review paper of Jin et al. [25] offers a comprehensive overview of the state of the art on these topics.

Despite these promises, accurate and efficient computation of dispersion curves and transient signals propagating through plates coupled to resonators often remains a challenge. Analytical solutions are typically limited to idealized cases, while direct numerical simulations, such as those based on finite element analysis, can become computationally prohibitive for large-scale or highly detailed models. Existing methods have addressed some of these limitations by leveraging simplifications such as equivalent homogenization approaches [26], multiple scattering formulations [27] or plane wave expansions approaches [28]. At present, WFE, and related reduced methods such as those based on Bloch mode synthesis [29], are arguably the most popular technique used by metamaterial researchers to produce dispersion curves of periodic structures.

To the best of the authors' knowledge, the SAFE method, which is somewhat popular in the NDE and SHM communities, has never been specialized to study plates (or other waveguides) equipped with resonators. As explained above, by reducing the wave analysis to a 1D or 2D problem, the SAFE approach can offer enormous computational advantages for all structural conditions exhibiting periodicity or translational invariance along one dimension. Importantly, apart from the computation of dispersion curves in terms of, e.g., wavenumbers and attenuation, SAFE is also well suited for the calculation of cross-sectional wave shapes and transient signals [30,31].

In this work, the SAFE method is extended to analyze guided waves propagating in plates equipped with resonators and potentially surrounded by fluids. In particular, the resonators are modeled in the SAFE framework via an effective medium approach valid for guided wave wavelengths larger than both resonators' dimensions and spacing. An isotropic and linear viscoelastic steel plate immersed in vacuum or in water and loaded by an infinite array of mass–spring–dashpot oscillators is considered to show the potential of the proposed formulation.

The remainder of the article is structured as follows. Section 2 derives the semi-analytical finite element formulation for a plate in vacuum or coupled to a fluid and loaded by infinite arrays of resonators. Section 3 presents and discusses some numerical examples. Finally, Section 4 concludes the article by highlighting the key findings.

2. Semi-analytical finite element formulation

The scenario of interest, depicted in Fig. 1(a), consists of a plate immersed in an inviscid fluid and coupled to an array of resonators on each outer surface. Note that in this article the term "plate" refers to a two-dimensional elastic waveguide, modeled as a solid medium in which guided waves can propagate, rather than a structural plate governed by classical plate theories that involve the bi-harmonic operator. This distinction aligns with the common usage in wave propagation studies, particularly in the context of Lamb waves. The generic layer of the plate has density ρ and supports longitudinal and shear waves traveling at speeds c_l and c_s, respectively. The fluid above and below the plate has density ρ_f and only supports longitudinal waves traveling at speed c_f. The system supports quasi-Lamb waves, which leak energy from the plate into the fluid, as well as quasi-Scholte waves, which propagate along the fluid–solid interface.

If the resonators coupled to either side of the plate are closely spaced, their collective dynamic response can be homogenized through an effective medium approach [32]. Such an approach is valid for wavelengths significantly larger than resonators dimensions and spacing between them, allowing the plate-resonator system to be treated as a continuous medium with frequency dependent boundary conditions.

In the following, a semi-analytical finite element formulation is used to describe the plate's thickness via finite elements, while both the arrays of homogenized resonators and the adjacent fluid are treated as Neumann boundary conditions, as indicated by the gray and cyan arrows representing tractions at the plate's outer surfaces in Fig. 1(b).

2.1. Numerical formulation

Let us consider elastic plane waves propagating along the x-direction on a plate decorated with resonators and immersed in an inviscid fluid. The system can be studied assuming the $x-z$ plane under plane-strain conditions. The reference system is that of

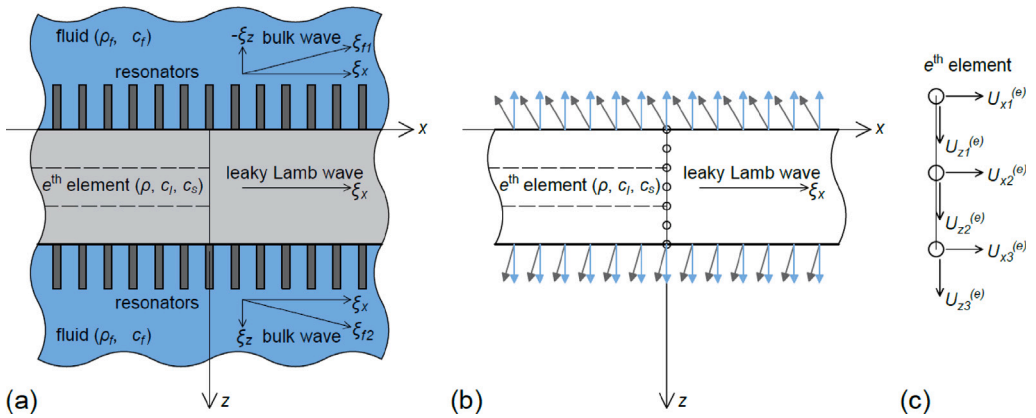

Fig. 1. Model of a plate immersed in an inviscid fluid and coupled to an infinite array of resonators at each external surface. (a) General physical scenario. (b) Fluid and resonators represented by tractions exerted on the plate. (c) Degrees of freedom for a one-dimensional three-node element.

Fig. 1. The plate can be composed of isotropic linear viscoelastic materials. Displacement ($\mathbf{u}$), strain ($\boldsymbol{\varepsilon}$), stress ($\boldsymbol{\sigma}$) and external traction ($\mathbf{t}$) vectors are expressed as:

$$\mathbf{u} = \begin{bmatrix} u_x \\ u_z \end{bmatrix}, \quad \boldsymbol{\varepsilon} = \begin{bmatrix} \varepsilon_{xx} \\ \varepsilon_{zz} \\ \gamma_{xz} \end{bmatrix}, \quad \boldsymbol{\sigma} = \begin{bmatrix} \sigma_{xx} \\ \sigma_{zz} \\ \tau_{xz} \end{bmatrix}, \quad \mathbf{t} = \mathbf{t}^{\text{res}} + \mathbf{t}^{\text{fluid}} = \begin{bmatrix} t_x \\ t_z \end{bmatrix} \tag{1}$$

where $\mathbf{t}^{\text{res}}$ and $\mathbf{t}^{\text{fluid}}$ identify the tractions exerted by resonators and fluid, respectively.

The plate's cross-sectional domain Ω lies on the y-z plane, and it is discretized by n_{el} three-node one-dimensional finite elements, each having domain Ω_e (shown in Fig. 1(c)). This results in a total of $n_{\text{nodes}} = 3 + (n_{\text{el}} - 1) \cdot 2$ nodes and $n_{\text{dof}} = 2 \cdot n_{\text{nodes}}$ degrees-of-freedom. Under harmonic waves with respect to both space x and time t, the displacement vector over the element domain $\mathbf{u}^{(e)}$ can be expressed in terms of shape functions $\mathbf{N}(z)$ and nodal displacements $\mathbf{U}^{(e)}$ as:

$$\mathbf{u}^{(e)} = \mathbf{N}(z)\mathbf{U}^{(e)} e^{\mathrm{i}(\xi_x x - \omega t)} \tag{2}$$

$$\mathbf{N}(z) = \begin{bmatrix} N_1 & 0 & N_2 & 0 & N_3 & 0 \\ 0 & N_1 & 0 & N_2 & 0 & N_3 \end{bmatrix} \tag{3}$$

$$\mathbf{U}^{(e)} = \begin{bmatrix} U_{x1} & U_{z1} & U_{x2} & U_{z2} & U_{x3} & U_{z3} \end{bmatrix}^T \tag{4}$$

where ξ_x is the wavenumber in the x-direction, ω is the angular frequency and T is the transpose operator.

The compatibility equations over the element domain reads:

$$\boldsymbol{\varepsilon}^{(e)} = \left[\mathbf{L}_x \frac{\partial}{\partial x} + \mathbf{L}_z \frac{\partial}{\partial z} \right] \mathbf{u}^{(e)}, \quad \mathbf{L}_x = \begin{bmatrix} 1 & 0 \\ 0 & 0 \\ 0 & 1 \end{bmatrix}, \quad \mathbf{L}_z = \begin{bmatrix} 0 & 0 \\ 0 & 1 \\ 1 & 0 \end{bmatrix} \tag{5}$$

hence the strain vector over the element domain $\boldsymbol{\varepsilon}^{(e)}$ can be expressed in terms of shape functions and nodal displacements as:

$$\boldsymbol{\varepsilon}^{(e)} = (\mathbf{B}_1 + \mathrm{i}\xi_x \mathbf{B}_2)\mathbf{U}^{(e)} e^{\mathrm{i}(\xi_x x - \omega t)}, \quad \mathbf{B}_1 = \mathbf{L}_z \mathbf{N}_{,z}, \quad \mathbf{B}_2 = \mathbf{L}_x \mathbf{N} \tag{6}$$

where $\mathbf{N}_{,z}$ is the derivative of the shape function matrix with respect to z.

The constitutive equations relate strains $\boldsymbol{\varepsilon}^{(e)}$ and stresses $\boldsymbol{\sigma}^{(e)}$ over the element domain as:

$$\boldsymbol{\sigma}^{(e)} = \tilde{\mathbf{C}}^{(e)} \boldsymbol{\varepsilon}^{(e)} \tag{7}$$

where $\tilde{\mathbf{C}}^{(e)}$ is the generally complex material's stiffness matrix. For a linear viscoelastic material subjected to time harmonic motions, the latter can be expressed as $\tilde{\mathbf{C}}^{(e)} = \tilde{\mathbf{C}}^{(e)\prime} - \mathrm{i}\tilde{\mathbf{C}}^{(e)\prime\prime}$, where $\tilde{\mathbf{C}}^{(e)\prime}$ and $\tilde{\mathbf{C}}^{(e)\prime\prime}$ contains storage and loss moduli, respectively.

Finally, the external traction vector over the element domain ($\mathbf{t}$) can also be expressed in terms of shape functions and the nodal external traction vector as:

$$\mathbf{t}^{(e)} = \mathbf{N}(z)\mathbf{T}^{(e)} e^{\mathrm{i}(\xi_x x - \omega t)} \tag{8}$$

The principle of virtual work for the eth element ($e = 1, 2, \ldots, n_{\text{el}}$) and for any pair of mutually-consistent virtual displacement ($\delta\mathbf{u}^{(\mathbf{e})}$) and strain ($\delta\boldsymbol{\varepsilon}^{(\mathbf{e})}$) vectors prescribes the following relation between the work done by the external traction and the increments of kinetic and potential energies:

$$\int_{B^{(e)}} \delta\mathbf{u}^{(\mathbf{e})^T} \mathbf{t}^{(\mathbf{e})} \, \mathrm{d}B^{(e)} = \int_{A^{(e)}} \delta\mathbf{u}^{(\mathbf{e})^T} (\rho^{(e)} \ddot{\mathbf{u}}^{(e)}) \, \mathrm{d}A^{(e)} + \int_{A^{(e)}} \delta\boldsymbol{\varepsilon}^{(e)^T} \boldsymbol{\sigma}^{(e)} \, \mathrm{d}A^{(e)} \tag{9}$$

where $\int_{B^{(e)}} \square \mathrm{d}B^{(e)}$ is the line integral over upper and lower boundaries of the element, $\int_{A^{(e)}} \square \mathrm{d}A^{(e)}$ is the surface integral over the element, $\rho^{(e)}$ is the density of the material, and the two dots over a term indicate second derivative with respect to time.

By expressing the virtual displacement and strain vectors as:

$$\delta\mathbf{u}^{(e)} = \mathbf{N}(z)\delta\mathbf{U}^{(e)}\mathrm{e}^{\mathrm{i}(-\xi_x x+\omega t)}, \quad \delta\boldsymbol{\varepsilon}^{(e)} = (\mathbf{B}_1 - \mathrm{i}\xi_x\mathbf{B}_2)\delta\mathbf{U}^{(e)}\mathrm{e}^{\mathrm{i}(-\xi_x x+\omega t)} \tag{10}$$

and by substituting Eqs. (2)–(8), (10) into Eq. (9), the latter yields:

$$\begin{aligned}\delta\mathbf{U}^{(\mathbf{e})T}\int_{B^{(e)}}\left[\mathbf{N}^T\mathbf{N}\right]\mathrm{d}B^{(e)}\mathbf{T}^{(\mathbf{e})} = &-\delta\mathbf{U}^{(\mathbf{e})T}\omega^2\int_{A^{(e)}}\left[\rho^{(e)}\mathbf{N}^T\mathbf{N}\right]\mathrm{d}A^{(e)}\mathbf{U}^{(\mathbf{e})}\\ &+\delta\mathbf{U}^{(\mathbf{e})T}\int_{A^{(e)}}\left[(\mathbf{B}_1^T - \mathrm{i}\xi_x\mathbf{B}_2^T)\tilde{\mathbf{C}}^{(e)}(\mathbf{B}_1 + \mathrm{i}\xi_x\mathbf{B}_2)\right]\mathrm{d}A^{(e)}\mathbf{U}^{(\mathbf{e})}\end{aligned} \tag{11}$$

After rewriting $\int_{B^{(e)}} \square \mathrm{d}B^{(e)} = \int_x \square \mathrm{d}x$ and $\int_{A^{(e)}} \square \mathrm{d}A^{(e)} = \int_x \int_{z_1^{(e)}}^{z_3^{(e)}} \square \mathrm{d}z\mathrm{d}x$, with $z_1^{(e)}$ and $z_3^{(e)}$ being the z coordinates of upper and lower nodes for the eth element, some algebraic manipulations yield:

$$\mathbf{F}^{(e)} = \left[\mathbf{K}_1^{(e)} + \mathrm{i}\xi_x\mathbf{K}_2^{(e)} + \xi_x^2\mathbf{K}_3^{(e)} - \omega^2\mathbf{M}^{(e)}\right]\mathbf{U}^{(e)} \tag{12}$$

where:

$$\begin{aligned}\mathbf{F}^{(e)} &= \begin{bmatrix}T_{x1}^{(e)} & T_{z1}^{(e)} & T_{x2}^{(e)} & T_{z2}^{(e)} & T_{x3}^{(e)} & T_{z3}^{(e)}\end{bmatrix}^T, \quad \mathbf{K}_1^{(e)} = \int_{z_1^{(e)}}^{z_3^{(e)}}\left[\mathbf{B}_1^T\tilde{\mathbf{C}}^{(e)}\mathbf{B}_1\right]\mathrm{d}z,\\ \mathbf{K}_2^{(e)} &= \int_{z_1^{(e)}}^{z_3^{(e)}}\left[\mathbf{B}_1^T\tilde{\mathbf{C}}^{(e)}\mathbf{B}_2 - \mathbf{B}_2^T\tilde{\mathbf{C}}^{(e)}\mathbf{B}_1\right]\mathrm{d}z, \quad \mathbf{K}_3^{(e)} = \int_{z_1^{(e)}}^{z_3^{(e)}}\left[\mathbf{B}_2^T\tilde{\mathbf{C}}^{(e)}\mathbf{B}_2\right]\mathrm{d}z,\\ \mathbf{M}^{(e)} &= \int_{z_1^{(e)}}^{z_3^{(e)}}\left[\rho^e\mathbf{N}^T\mathbf{N}\right]\mathrm{d}z\end{aligned} \tag{13}$$

By applying standard finite element assembling procedures to Eq. (12) the following system of governing equations is obtained:

$$\mathbf{F} = \left[\mathbf{K}_1 + \mathrm{i}\xi_x\mathbf{K}_2 + \xi_x^2\mathbf{K}_3 - \omega^2\mathbf{M}\right]\mathbf{U} \tag{14}$$

$$\mathbf{U} = \begin{bmatrix}U_{x1} & U_{z1} & \cdots & U_{xn_{\mathrm{nodes}}} & U_{zn_{\mathrm{nodes}}}\end{bmatrix}^T \tag{15}$$

$$\mathbf{F} = \mathbf{F}^{\mathrm{res}} + \mathbf{F}^{\mathrm{fluid}} = \begin{bmatrix}T_{x1} & T_{z1} & \cdots & T_{xn_{\mathrm{nodes}}} & T_{zn_{\mathrm{nodes}}}\end{bmatrix}^T \tag{16}$$

where $\mathbf{K}_1$, $\mathbf{K}_2$, $\mathbf{K}_3$ and $\mathbf{M}$ are $n_{\mathrm{dof}} \times n_{\mathrm{dof}}$ matrices, while $\mathbf{U}$, $\mathbf{F}$, $\mathbf{F}^{\mathrm{res}}$ and $\mathbf{F}^{\mathrm{fluid}}$ are n_{dof} vectors, with the latter two expressing the external forces applied to the plate by resonators and fluid, respectively.

Eq. (14) can be formulated as a homogeneous system by expressing the interaction of the plate with both fluid and resonators as boundary conditions, as shown in the following.

2.1.1. Boundary conditions due to the resonators

The force exerted by the resonators can be expressed as:

$$\mathbf{F}^{\mathrm{res}} = \begin{bmatrix}\mathbf{T}^{\mathrm{res}(1)}(\omega) & 0 & \cdots & 0 & \mathbf{T}^{\mathrm{res}(2)}(\omega)\end{bmatrix}^T \tag{17}$$

with:

$$\begin{aligned}\mathbf{T}^{\mathrm{res}(1)}(\omega) &= \begin{bmatrix}Z_{11}^{\mathrm{res}(1)} & Z_{12}^{\mathrm{res}(1)}\\ Z_{21}^{\mathrm{res}(1)} & Z_{22}^{\mathrm{res}(1)}\end{bmatrix}\begin{bmatrix}U_{x1}\\ U_{z1}\end{bmatrix} = \mathbf{Z}^{\mathrm{res}(1)}(\omega)\mathbf{U}_1,\\ \mathbf{T}^{\mathrm{res}(2)}(\omega) &= \begin{bmatrix}Z_{11}^{\mathrm{res}(2)} & Z_{12}^{\mathrm{res}(2)}\\ Z_{21}^{\mathrm{res}(2)} & Z_{22}^{\mathrm{res}(2)}\end{bmatrix}\begin{bmatrix}U_{xn_{\mathrm{nodes}}}\\ U_{zn_{\mathrm{nodes}}}\end{bmatrix} = \mathbf{Z}^{\mathrm{res}(2)}(\omega)\mathbf{U}_{n_{\mathrm{nodes}}}\end{aligned} \tag{18}$$

where $\mathbf{Z}^{\mathrm{res}(1)}(\omega)$ and $\mathbf{Z}^{\mathrm{res}(2)}(\omega)$ represent the mechanical impedance offered by the homogenized resonators coupled to upper and lower surfaces of the plate, respectively.

Eq. (17) can be rewritten in a compact form as:

$$\mathbf{F}^{\mathrm{res}} = \mathbf{Z}(\omega)\mathbf{U} \tag{19}$$

with:

$$\mathbf{Z}(\omega) = \begin{bmatrix}Z_{11}^{\mathrm{res}(1)} & Z_{12}^{\mathrm{res}(1)} & \cdots & 0 & 0\\ Z_{21}^{\mathrm{res}(1)} & Z_{22}^{\mathrm{res}(1)} & \cdots & 0 & 0\\ \vdots & \vdots & \ddots & \vdots & \vdots\\ 0 & 0 & \cdots & Z_{11}^{\mathrm{res}(2)} & Z_{12}^{\mathrm{res}(2)}\\ 0 & 0 & \cdots & Z_{21}^{\mathrm{res}(2)} & Z_{22}^{\mathrm{res}(2)}\end{bmatrix} \tag{20}$$

As an example, the expression of $\mathbf{Z}(\omega)$ for the case of a plate whose upper surface is coupled to an homogenized array of mass–spring–dashpot oscillators with mass m_o, stiffness k_o and damping coefficient c_o is derived in the following. The governing dynamic equilibrium equation for the oscillator at the generic x-position reads:

$$m_o\ddot{u}_o + c_o(\dot{u}_o - \dot{U}_{z1}) + k_o(u_o - U_{z1}) = 0 \tag{21}$$

where u_o denotes the oscillator's mass absolute displacement in the z-direction. By assuming a time-harmonic motion occurring at a frequency ω:

$$U_{z1}(t) = \hat{u}_z e^{i\omega t}, \quad u_o(t) = \hat{u}_o e^{i\omega t} \tag{22}$$

the time derivatives become:

$$\dot{U}_{z1}(t) = i\omega\hat{u}_z e^{i\omega t}, \quad \dot{u}_o(t) = i\omega\hat{u}_o e^{i\omega t}, \quad \ddot{u}_o(t) = -\omega^2\hat{u}_o e^{i\omega t} \tag{23}$$

The substitution of Eq. (23) into Eq. (21), followed by minor algebraic manipulations, yields:

$$\hat{u}_o = \frac{(i\omega c_o + k_o)}{-\omega^2 m_o + i\omega c_o + k_o}\hat{u}_z \tag{24}$$

Therefore, the traction exerted by the oscillator to the plate can be expressed as:

$$T_{z1} = m_o\omega^2\hat{u}_o = \frac{m_o\omega^2(i\omega c_o + k_o)}{-\omega^2 m_o + i\omega c_o + k_o}\hat{u}_z \tag{25}$$

Finally, $\mathbf{Z}(\omega)$ specialized to the case of an infinite array of mass–spring–dashpot oscillators coupled to the plate's upper surface results in:

$$\mathbf{Z}(\omega) = \begin{bmatrix} 0 & 0 & \cdots & 0 \\ 0 & \frac{m_o\omega^2(i\omega c_o + k_o)}{-\omega^2 m_o + i\omega c_o + k_o} & \cdots & 0 \\ \vdots & \vdots & \ddots & 0 \\ 0 & 0 & 0 & 0 \end{bmatrix} \tag{26}$$

2.1.2. Boundary conditions due to the fluid

For any guided wave mode propagating in the plate with wavenumber ξ_x, pressure waves with wavevectors $\boldsymbol{\xi}_{f1}$ and $\boldsymbol{\xi}_{f2}$ are excited within the fluid media above and below the plate. For continuity of the displacement field, the x-components of $\boldsymbol{\xi}_{f1}$ and $\boldsymbol{\xi}_{f2}$, denoted $\xi_{f1,x}$ and $\xi_{f2,x}$, must match ξ_x, hence the z-components of $\boldsymbol{\xi}_{f1}$ and $\boldsymbol{\xi}_{f2}$, denoted $\xi_{f1,z}$ and $\xi_{f2,z}$, obey to:

$$\xi_z = -\xi_{f1,z} = \xi_{f2,z} = \sqrt{\xi_f^2 - \xi_x^2} \tag{27}$$

where:

$$\xi_x = \xi_{f,x}, \quad \xi_f = |\boldsymbol{\xi}_{f1}| = |\boldsymbol{\xi}_{f2}| = \frac{\omega}{c_f} \tag{28}$$

Under these conditions, the force exerted by the fluids to the plate's boundaries can be expressed as [31,33,34]:

$$\mathbf{F}^{\text{fluid}} = \begin{bmatrix} 0 & T^{f1}(\omega) & 0 & \cdots & 0 & T^{f2}(\omega) \end{bmatrix}^T \tag{29}$$

with:

$$T^{f1}(\omega) = \frac{i\rho_{f1}\omega^2}{\xi_z}U_{z1}, \quad T^{f2}(\omega) = \frac{i\rho_{f2}\omega^2}{\xi_z}U_{zn_{\text{nodes}}} \tag{30}$$

where ρ_{f1} and ρ_{f2} refer to the fluid medium above and below the plate, respectively, and they are here introduced as two distinct variables so that the formulation that will be derived in the following can be specialized to having the fluid medium only on one side of the plate by setting either ρ_{f1} or ρ_{f2} to zero.

By introducing the following matrix:

$$\mathbf{Q} = \begin{bmatrix} 0 & 0 & \cdots & 0 & 0 \\ 0 & \rho_{f1} & \cdots & 0 & 0 \\ \vdots & \vdots & \ddots & \vdots & \vdots \\ 0 & 0 & \cdots & 0 & 0 \\ 0 & 0 & \cdots & 0 & \rho_{f2} \end{bmatrix} \tag{31}$$

Eq. (29) can be rewritten as:

$$\mathbf{F}^{\text{fluid}} = i\frac{\omega^2}{\xi_z}\mathbf{Q}\mathbf{U} \tag{32}$$

2.2. Formulation and solutions of the generalized eigenvalue problem

Equipped with the previously-derived expressions of the forces exerted by resonators (Eq. (19)) and fluid (Eq. (32)), Eq. (14) can be rewritten as:

$$\left[\mathbf{K}_1 + \mathrm{i}\xi_x\mathbf{K}_2 + \xi_x^2\mathbf{K}_3 - \omega^2\mathbf{M} - \mathbf{Z}(\omega) - \mathrm{i}\frac{\omega^2}{\xi_z}\mathbf{Q}\right]\mathbf{U} = \mathbf{0} \tag{33}$$

Note that, under the assumption of subwavelength resonator dimensions/spacing, Eq. (33) neglects any possible direct interaction between the resonators and the fluid medium when both a metasurface and a fluid medium are simultaneously present on either side of the plate.

Eq. (33) can be expressed as a linear generalized eigenvalue problem by following an analogous procedure as that originally laid out by Hayashi and Inoue [31]. Such procedure will be applied to the case at hand by also correcting a few sign errors that were identified in the original work.

Let us first rearrange the terms within $\mathbf{U}$ and within all matrices appearing in Eq. (33) such that the x-displacements appear before the z-displacements (e.g., $\mathbf{K}_1 = \begin{bmatrix}\mathbf{K}_{1x} & \mathbf{K}_{1z}\end{bmatrix}$). Let us then rewrite Eq. (33) in terms of its mth solution considering, at first, the wave propagating towards the positive x-direction, i.e., the eigenvalues ξ_{xm} and ξ_{zm} (which satisfy Eq. (27)), with corresponding eigenvector $\boldsymbol{\phi}_m^+ = \begin{bmatrix}\boldsymbol{\phi}_{xm} & \boldsymbol{\phi}_{zm}\end{bmatrix}^T$:

$$\begin{aligned}\Big\{&\begin{bmatrix}\mathbf{K}_{1x} & \mathbf{K}_{1z}\end{bmatrix} + \mathrm{i}\xi_{xm}\begin{bmatrix}\mathbf{K}_{2x} & \mathbf{K}_{2z}\end{bmatrix} + \xi_{xm}^2\begin{bmatrix}\mathbf{K}_{3x} & \mathbf{K}_{3z}\end{bmatrix} - \omega^2\begin{bmatrix}\mathbf{M}_x & \mathbf{M}_z\end{bmatrix}\\ &- \begin{bmatrix}\mathbf{Z}_x(\omega) & \mathbf{Z}_z(\omega)\end{bmatrix} - \mathrm{i}\frac{\omega^2}{\xi_{zm}}\begin{bmatrix}\mathbf{Q}_x & \mathbf{Q}_z\end{bmatrix}\Big\}\begin{bmatrix}\boldsymbol{\phi}_{xm}\\ \boldsymbol{\phi}_{zm}\end{bmatrix} = 0\end{aligned} \tag{34}$$

For symmetry in $\pm x$-directions, Eq. (33) is also satisfied by the eigenvalues $-\xi_{xm}$ and ξ_{zm} (which again satisfy Eq. (27)), with corresponding eigenvector $\boldsymbol{\phi}_m^- = \begin{bmatrix}-\boldsymbol{\phi}_{xm} & \boldsymbol{\phi}_{zm}\end{bmatrix}^T$, hence the following equation also holds:

$$\begin{aligned}\Big\{&\begin{bmatrix}\mathbf{K}_{1x} & \mathbf{K}_{1z}\end{bmatrix} - \mathrm{i}\xi_{xm}\begin{bmatrix}\mathbf{K}_{2x} & \mathbf{K}_{2z}\end{bmatrix} + \xi_{xm}^2\begin{bmatrix}\mathbf{K}_{3x} & \mathbf{K}_{3z}\end{bmatrix} - \omega^2\begin{bmatrix}\mathbf{M}_x & \mathbf{M}_z\end{bmatrix}\\ &- \begin{bmatrix}\mathbf{Z}_x(\omega) & \mathbf{Z}_z(\omega)\end{bmatrix} - \mathrm{i}\frac{\omega^2}{\xi_{zm}}\begin{bmatrix}\mathbf{Q}_x & \mathbf{Q}_z\end{bmatrix}\Big\}\begin{bmatrix}-\boldsymbol{\phi}_{xm}\\ \boldsymbol{\phi}_{zm}\end{bmatrix} = 0\end{aligned} \tag{35}$$

Noting that in Eqs. (34), (35) $\mathbf{Q}_x = 0$, and computing:

$$\frac{\text{Eq. (34)} + \text{Eq. (35)}}{2} + \xi_{xm}\frac{\text{Eq. (34)} - \text{Eq. (35)}}{2} \tag{36}$$

the following expression is obtained:

$$\left[\mathbf{H}_{11} + \xi_{xm}^2\mathbf{H}_{12} - \mathrm{i}\frac{\omega^2}{\xi_{zm}}\mathbf{Q}\right]\boldsymbol{\phi}'_m = 0 \tag{37}$$

where:

$$\begin{aligned}\mathbf{H}_{11} &= \begin{bmatrix}\mathbf{K}_{1x} + \mathrm{i}\mathbf{K}_{2x} & \mathbf{K}_{1z}\end{bmatrix} - \omega^2\begin{bmatrix}\mathbf{M}_x & \mathbf{M}_z\end{bmatrix} - \begin{bmatrix}\mathbf{Z}_x(\omega) & \mathbf{Z}_z(\omega)\end{bmatrix},\\ \mathbf{H}_{12} &= \begin{bmatrix}\mathbf{K}_{3x} & \mathrm{i}\mathbf{K}_{2z} + \mathbf{K}_{3z}\end{bmatrix}, \quad \boldsymbol{\phi}'_m = \begin{bmatrix}\xi_{xm}\boldsymbol{\phi}_{xm}\\ \boldsymbol{\phi}_{zm}\end{bmatrix}\end{aligned} \tag{38}$$

The substitution of Eq. (27) into Eq. (37), with some rearrangements, results in the following 3rd-order polynomial generalized eigenvalue problem:

$$\begin{aligned}&\left[\mathbf{H}_0 + \xi_{zm}\mathbf{H}_1 + \xi_{zm}^3\mathbf{H}_3\right]\boldsymbol{\phi}'_m = 0,\\ &\mathbf{H}_0 = -\mathrm{i}\omega^2\mathbf{Q}, \quad \mathbf{H}_1 = \mathbf{H}_{11} + \xi_f^2\mathbf{H}_{12}, \quad \mathbf{H}_3 = -\mathbf{H}_{12}\end{aligned} \tag{39}$$

Eq. (39) can be recast into a linear eigenvalue problem as:

$$\left[\begin{bmatrix}\mathbf{0} & \mathbf{H}_1 & \mathbf{H}_0\\ \mathbf{I} & \mathbf{0} & \mathbf{0}\\ \mathbf{0} & \mathbf{I} & \mathbf{0}\end{bmatrix} - \xi_{zm}\begin{bmatrix}-\mathbf{H}_3 & \mathbf{0} & \mathbf{0}\\ \mathbf{0} & \mathbf{I} & \mathbf{0}\\ \mathbf{0} & \mathbf{0} & \mathbf{I}\end{bmatrix}\right]\begin{bmatrix}\xi_{zm}^2\boldsymbol{\phi}'_m\\ \xi_{zm}\boldsymbol{\phi}'_m\\ \boldsymbol{\phi}'_m\end{bmatrix} = \mathbf{0} \tag{40}$$

Finally, the dimensions of Eq. (40) can be reduced by removing the null-columns of $\mathbf{H}_0$, thus obtaining:

$$\begin{aligned}&\left[\begin{bmatrix}\mathbf{0} & \mathbf{H}_1 & \mathbf{H}'_0\\ \mathbf{I} & \mathbf{0} & \mathbf{0}\\ \mathbf{0} & \mathbf{I}' & \mathbf{0}\end{bmatrix} - \xi_{zm}\begin{bmatrix}-\mathbf{H}_3 & \mathbf{0} & \mathbf{0}\\ \mathbf{0} & \mathbf{I} & \mathbf{0}\\ \mathbf{0} & \mathbf{0} & \mathbf{I}''\end{bmatrix}\right]\begin{bmatrix}\xi_{zm}^2\boldsymbol{\phi}'_m\\ \xi_{zm}\boldsymbol{\phi}'_m\\ \boldsymbol{\phi}''_m\end{bmatrix} = \mathbf{0},\\ &\mathbf{H}'_0 = -\mathrm{i}\omega^2\mathbf{Q}', \quad \mathbf{Q}' = \begin{bmatrix}0 & \cdots & \rho_{f1} & \cdots & 0\\ 0 & \cdots & 0 & \cdots & \rho_{f2}\end{bmatrix}^T, \quad \mathbf{I}' = \begin{bmatrix}0 & \cdots & 1 & \cdots & 0\\ 0 & \cdots & 0 & \cdots & 1\end{bmatrix},\\ &\mathbf{I}'' = \begin{bmatrix}1 & 0\\ 0 & 1\end{bmatrix}, \quad \boldsymbol{\phi}''_m = \begin{bmatrix}\phi'_{m(\frac{n_{\mathrm{dof}}}{2}+2)}\\ \phi'_{m(n_{\mathrm{dof}})}\end{bmatrix}\end{aligned} \tag{41}$$

where the only non-zero columns of $(\mathbf{Q}')^T$ and $\mathbf{I}'$ are those with indexes $(n_{\mathrm{dof}}/2+2)$ and (n_{dof}).

Table 1
Material properties of the plate.

Density, ρ [kg m^{-3}]	Long. bulk speed, c_l [m s^{-1}]	Shear bulk speed, c_s [m s^{-1}]	Long. bulk attenuation [Np λ^{-1}]	Shear bulk attenuation [Np λ^{-1}]
7700	5960	3260	0.003	0.008

For any given ω, Eq. (41) can be seen as a linear generalized eigenvalue problem with respect to the wavenumber ξ_z. By solving it, $(2 \cdot n_{\text{dof}} + 2)$ eigenvalues ξ_z and corresponding eigenvectors are obtained. Finally, for every ξ_{zm}, a pair of positive and negative eigenvalues ξ_{xm} corresponding to the mth plate-like wave mode propagating in the $\pm x$ directions is obtained as:

$$\xi_{xm} = \pm\sqrt{\xi_f^2 - \xi_{zm}^2} \tag{42}$$

The real part of the wavenumber $\xi_{xm,\text{Re}}$ can be used to evaluate the phase velocity as $c_{\text{ph}} = \omega/\xi_{xm,\text{Re}}$, while the imaginary part $\xi_{xm,\text{Im}}$ gives the attenuation in Nepers per meter.

Note that two of the $(2 \cdot n_{\text{dof}} + 2)$ solutions yield by Eq. (41) correspond to quasi-Scholte modes.

By testing Eq. (41) on several numerical examples, the authors noticed that such equation can suffer from numerical instabilities, particularly for problems involving a large number of degrees of freedom and for high ω values. When this occurs, the authors also found that the instabilities can be eliminated by balancing the two matrices involved in the generalized eigenvalue problem of Eq. (41) via Ward's algorithm [35].

2.2.1. Solutions for resonator-coupled plates in vacuum

For resonator-coupled plates in vacuum (i.e., not surrounded by fluids) the external force vector reduces to $\mathbf{F} = \mathbf{F}^{\text{res}}$, hence Eq. (33) simplifies to:

$$\left[\mathbf{K}_1 + \mathrm{i}\xi_x\mathbf{K}_2 + \xi_x^2\mathbf{K}_3 - \omega^2\mathbf{M} - \mathbf{Z}(\omega)\right]\mathbf{U} = \mathbf{0} \tag{43}$$

Eq. (43) can be solved by adopting a procedure analogous to the well-known one for traction-free plates (see, e.g., [10]). First, the imaginary unit in Eq. (43) can be eliminated by introducing the $n_{\text{dof}} \times n_{\text{dof}}$ transformation matrix $\mathbf{D} = \text{diag}\left[\mathrm{i} \quad 1 \quad \mathrm{i} \quad 1 \quad \cdots \quad \mathrm{i} \quad 1\right]$, which has the properties $\mathbf{D}^T = \mathbf{D}^*$, where $()^*$ indicates complex conjugate, and $\mathbf{D}^*\mathbf{D} = \mathbf{D}\mathbf{D}^* = \mathbf{I}$, where $\mathbf{I}$ is the identity matrix. All terms of Eq. (43) are pre-multiplied by $\mathbf{D}^T$ and post-multiplied by $\mathbf{D}$. This operation does not alter any term except $\mathbf{K}_2$ (see [10] for a detailed explanation) and, possibly, $\mathbf{Z}(\omega)$ (it only alters it when either or both of $\mathbf{Z}^{\text{res}(1)}(\omega)$ and $\mathbf{Z}^{\text{res}(2)}(\omega)$ are non-diagonal), for which:

$$\mathbf{D}^T\mathbf{K}_2\mathbf{D} = -\mathrm{i}\hat{\mathbf{K}}_2, \quad \mathbf{D}^T\mathbf{Z}(\omega)\mathbf{D} = \hat{\mathbf{Z}}(\omega) \tag{44}$$

Then, Eq. (43) becomes:

$$\left[\mathbf{K}_1 + \xi_x\hat{\mathbf{K}}_2 + \xi_x^2\mathbf{K}_3 - \omega^2\mathbf{M} - \hat{\mathbf{Z}}(\omega)\right]\hat{\mathbf{U}} = \mathbf{0} \tag{45}$$

where $\hat{\mathbf{U}}$ is a new nodal displacement vector.

For a given angular frequency ω, which is a real positive quantity, Eq. (45) can be seen as a nonlinear generalized eigenvalue problem with respect to the wavenumber ξ_x. The latter is generally complex, and can have both positive and negative signs. Notably, Eq. (45) can be linearized by recasting it to a first-order eigensystem by doubling its algebraic size as:

$$\left[\mathbf{A} - \xi_x\mathbf{B}\right]\mathbf{V} = \mathbf{0} \tag{46}$$

$$\mathbf{A} = \begin{bmatrix} \mathbf{0} & \mathbf{K}_1 - \omega^2\mathbf{M} - \hat{\mathbf{Z}}(\omega) \\ \mathbf{K}_1 - \omega^2\mathbf{M} - \hat{\mathbf{Z}}(\omega) & \hat{\mathbf{K}}_2 \end{bmatrix}, \quad \mathbf{B} = \begin{bmatrix} \mathbf{K}_1 - \omega^2\mathbf{M} - \hat{\mathbf{Z}}(\omega) & \mathbf{0} \\ \mathbf{0} & -\mathbf{K}_3 \end{bmatrix}, \quad \mathbf{V} = \begin{bmatrix} \mathbf{U} \\ \xi_x\mathbf{U} \end{bmatrix} \tag{47}$$

where $\mathbf{A}$ and $\mathbf{B}$ are $(2 \cdot n_{\text{dof}}) \times (2 \cdot n_{\text{dof}})$ matrices, while $\mathbf{V}$ is a $(2 \cdot n_{\text{dof}})$ vector. For any given ω, $(2 \cdot n_{\text{dof}})$ eigenvalues ξ_x with corresponding $(2 \cdot n_{\text{dof}})$ eigenvectors are obtained, representing modes propagating in the $\pm x$ directions.

3. Numerical examples

3.1. Steel plate in vacuum coupled to an infinite array of mass–spring–dashpot oscillators at its top surface

A 1 mm-thick steel plate in vacuum with material properties as in Table 1 was discretized using 20 one-dimensional three-node elements, for a total of 41 nodes and 82 degrees of freedom. The plate is coupled to an infinite array of mass–spring–dashpot oscillators at its top surface. The oscillators have homogenized mass $m_o = 7.7$ kg/m^2, damping coefficient $c_o = 0$ and resonant frequency $f_o = 1$ MHz. Such resonant frequency was chosen as to be lower than the cut-on of the Lamb A1 mode existing in the absence of oscillators.

The eigenvalue problem of Eqs. (46), (47), with $\hat{\mathbf{Z}}(\omega)$ expressed as $\mathbf{Z}(\omega)$ of Eq. (26), was solved at a range of ω values, and Fig. 2(a–c) shows the resulting (a) "Wavenumber vs. frequency", (b) "Frequency vs. phase velocity" and (c) "Frequency vs. attenuation" dispersion curves in black lines. Four modes are visible in the plots, which are denoted m_1 to m_4 (note that m_4 is not visible at

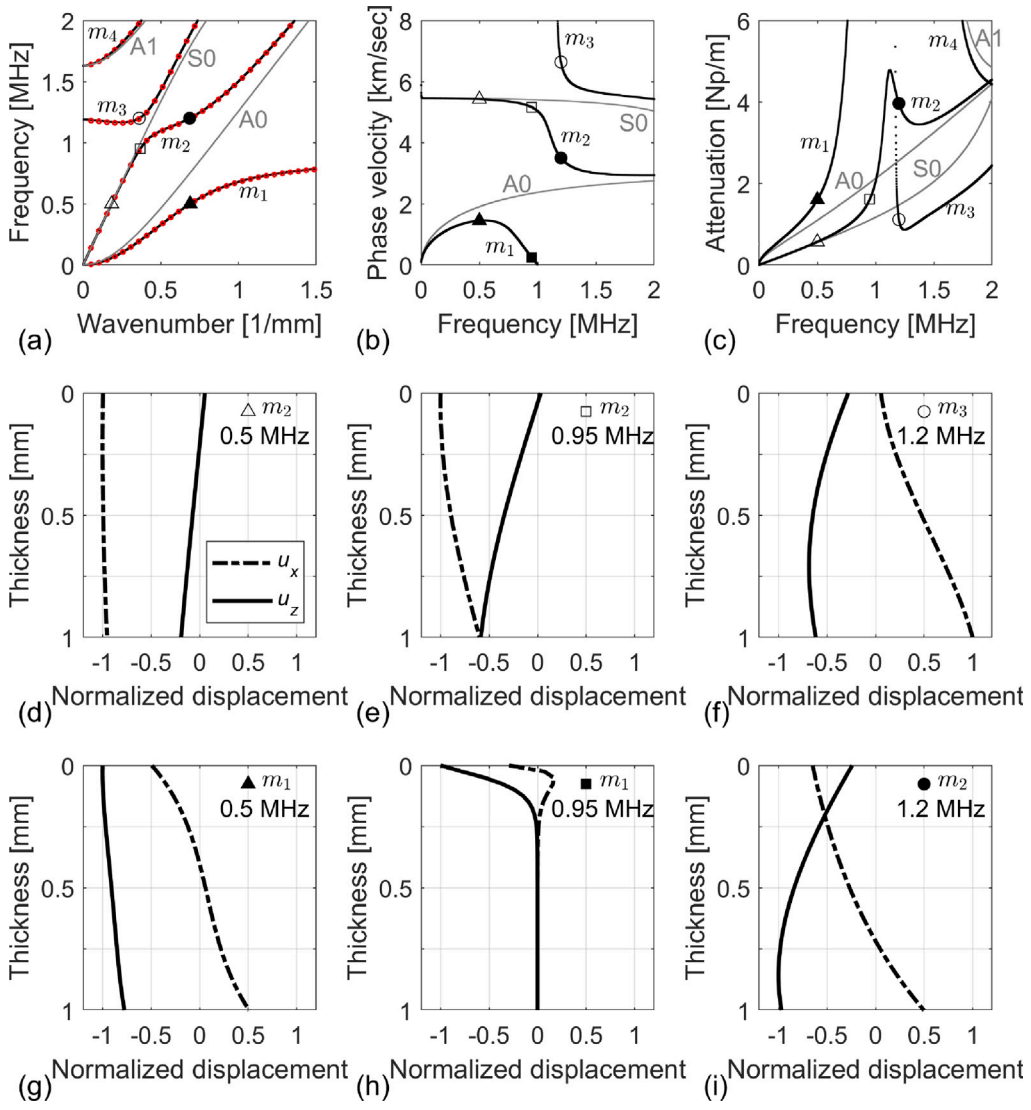

Fig. 2. 1 mm-thick steel plate in vacuum with material properties as in Table 1 and coupled to an array of homogenized oscillators with homogenized mass $m_o = 7.7$ kg/m^2, damping coefficient $c_o = 0$ and resonant frequency $f_o = 1$ MHz. (a) "Wavenumber vs. frequency", (b) "Phase velocity vs. frequency" and (c) "Attenuation vs. frequency" dispersion curves (black lines), compared to those obtained in the absence of resonators (gray lines); the red markers indicate the solutions obtained via the wave finite element (WFE) method (details of its implementation given in Appendix A); the six black markers pinpoint the solutions for which the corresponding wave shapes are plotted in (d–i) (the filled square marker is out-of-scale in plots (a) and (c)). (d–i) Cross-sectional displacement wave shapes.

the zoom-level of plot (b)). The red markers in plot (a) represent the solutions obtained on an analogous problem implemented in COMSOL Multiphysics and solved via the WFE method [6] in order to verify the results. The details of the WFE implementation are given in Appendix A. The solutions provided by the two numerical approaches are in excellent agreement. Fig. 2(a–c) also plots in gray lines the dispersion curves obtained by solving Eqs. (46), (47) in the absence of resonators (i.e., by setting $\hat{\mathbf{Z}}(\omega) = \mathbf{0}$), and these correspond to A0, S0 and A1 modes (with A1 being out-of-scale in plot (b)). Finally, the six black markers in Fig. 2(a–c) indicate the modal solutions for the resonator-coupled plate at 0.5 (triangles), 0.95 (squares) and 1.2 (circles) MHz, whose modal shapes are plotted in Fig. 2(d–i). Note that the filled square marker is out-of-scale in plots (a) and (c).

The comparison of black and gray lines of Fig. 2(a–c) facilitates the interpretation of the physical scenarios. At very low frequencies, m_1 behaves as A0. As the frequency grows, the black line corresponding to m_1 in each of the three plots keeps deviating from the actual A0 of the traction-free scenario. Then, as the frequency approaches the resonant frequency of the oscillators $f_o = 1$ MHz, the m_1 line in plot (a) plateaus towards f_o at ever-increasing wavenumbers, and this corresponds to its phase velocity getting to zero (plot (b)) and to its attenuation growing steeply to very large numbers (plot (c)).

The cross-sectional wave shapes of m_1 at 0.5 and 0.95 MHz are plotted in Fig. 2(g,h). At 0.5 MHz (plot (g)) the wave shape still resembles that of an A0 mode, though it is already noticeable that the out-of-plane displacement (solid line, marked as u_z)

is not perfectly antisymmetric. At 0.95 MHz (plot (h)) both out-of-plane and in-plane displacements (the latter being plotted as dash-dotted line, marked as u_x) are almost entirely localized at the upper surface of the plate, with such displacements dictated by the oscillators' resonance. On these conditions, this mode cannot propagate, as already evidenced by its phase velocity and attenuation curves tending to zero and to a very large value, respectively.

Let us now consider mode m_2. At low frequencies, this mode behaves as S0. However, also in this case, as frequency grows towards $f_o = 1$ MHz the black lines corresponding to m_2 deviate from S0, and then actually tend towards the gray lines corresponding to A0 at higher frequencies. The wave shapes of m_2 at 0.5, 0.95, and 1.2 MHz are plotted in Fig. 2(d,e,i). At 0.5 MHz (plot (d)), the m_2's wave shape still resembles that of S0, though the out-of-plane displacement is non-symmetric. At 0.95 MHz (plot (e)), the out-of-plane displacement is essentially null at the oscillator-coupled upper surface, and increases in the direction of the bottom surface. Instead, in-plane displacements exist across the whole thickness, although they are now diverging from being symmetric. At frequencies higher than the oscillators' resonant frequency, out-of-plane displacements at the upper plate's surface can again support the wave propagation, hence the wave shape at 1.2 MHz (plot (i)) shows a non-zero u_z at the top of the plot. Concurrently, the in-plane displacements are now significantly non-symmetric.

At a frequency higher than f_o (i.e., at ~1.19 MHz), a mode denoted m_3 cut-on in the oscillators-coupled scenario. Its wave shape at 1.2 MHz (empty circle in Fig. 2(a–c)) is plotted in Fig. 2(f). The plot shows that the in-plane displacements are mostly occurring towards the bottom half of the plate and are almost null at the top surface, while its out-of-plane motions are almost antisymmetric, therefore vaguely resembling the modal shapes of A0. Then, as frequency grows to larger value, the black lines of Fig. 2(a–c) corresponding to m_3 tend towards those of S0.

Finally, the modes cutting-on at ~1.63 MHz in Fig. 2(a,c) are A1 and its corresponding one, denoted m_4, respectively for the scenarios without and with the oscillators.

3.1.1. Transfer functions and transient signals at varying propagation distances

The dispersion curves describe the propagation characteristics in an infinitely long waveguide. However, this information only provides a partial description of real-world cases, where interfaces with metamaterials are generally of finite size. The study of wave propagation in such cases would be greatly aided by the possibility of plotting the transfer functions relating a given set of unitary forces applied at some plate's "transmitter" location and the nodal displacements at a desired "receiver" location. The SAFE formulation presented in Section 2.2.1 is well suited to these scopes. In fact, once the matrices $\mathbf{A}$ and $\mathbf{B}$ of Eqs. (46), (47) are constructed for the case of a metasurface represented by a given matrix $\hat{\mathbf{Z}}(\omega)$, it is then possible to use the same procedure outlined in [30,36] to compute the transfer functions, as well as the transient signals that would be obtained when specific forcing time-histories are considered.

An example of these capabilities is given in this section, where the same oscillator-coupled plate studied in the previous section is considered. Fig. 3(a) re-plots the "Wavenumber vs. frequency" dispersion curves of Fig. 2(a) in a semi-logarithmic scale. Fig. 3(b–c) display the transfer functions associated to an A0-type of excitation (i.e., uniform out-of-plane force applied to all nodes in the plate's cross section), for receivers measuring the out-of-plane displacements at either (b) the top or (c) the bottom surface of the plate, and at three different propagation distances of either 100, 500 or 900 times the plate's thickness (i.e., 100, 500 or 900 mm). Note that each graph in the figure was obtained by normalizing each transfer function by the equivalent function obtained for the traction-free plate scenario (i.e., in the absence of oscillators). Fig. 3(b), which considers the out-of-plane motion at the plate's top surface, shows a significant dip at exactly 1 MHz (i.e., at the oscillators' resonant frequency), and for all propagation distances. Based on the discussion in the previous section, this is expected, since m_1 does not propagate at this frequency (being highly attenuated and with a null-phase velocity), while m_2 propagates with a null-u_z displacement at the top surface, as indicated in Fig. 2(e). Indeed, Fig. 3(c) does not exhibit an analogous dip at 1 MHz, since m_2 propagates at that frequency with non-null u_z displacements towards the bottom half of the plate's cross-section. Fig. 3(b) also shows that due to the strong attenuation of m_1 at frequencies higher than ~0.6 MHz (Fig. 2(c)), at increasing propagation distances there is an increasingly wider frequency-band below $f_o = 1$ MHz that is characterized by a very low amplitude. Again, this phenomenon is significantly less pronounced in Fig. 3(c), since m_2 does propagate across that frequency range with relatively low attenuation. Finally, both plots (b,c) show the effects of the appearance of m_3 at and above its cut-on frequency of ~1.19 MHz.

As previously mentioned, transient signals can also be computed. For example, Figs. 4 and 5 show the signals that would be sensed by receivers measuring the out-of-plane displacement at the plate's top surface at distances of 100, 500 or 900 times the plate's thickness from the source, the latter being an A0-type of excitation corresponding to a Hann-windowed pulse comprising 10 cycles centered at 0.75 and 0.95 MHz, respectively for Figs. 4 and 5. This is the same transmitter/receiver configuration of Fig. 3(b), where the green dashed and dash-dotted lines indicate frequencies of 0.75 and 0.95 MHz, respectively. In each of Figs. 4 and 5, both time–history and frequency content of the pulses are displayed in plots (a,b), while plot (c) superposes the signals measured at the three propagation distances in the traction-free plate scenario, and each of plots (d–f) considers a single propagation distance for the plate loaded by the oscillators. Note that in each figure all motion amplitudes are normalized to the highest value seen in the traction-free plate scenario for a distance of 100 mm, and that the time-scale of plots (c) is much smaller than that of plots (d–f).

Let us first restrict the attention to the 0.75 MHz excitation, i.e., to Fig. 4. As expected, in the traction-free plate scenario when the forcing excitation is applied uniformly through-thickness in the out-of-plane direction only the A0 mode is excited, and this corresponds to the three arrivals seen in Fig. 4(c), whose amplitudes decrease at increasing propagation distances due to both material attenuation and dispersion effects. When the plate is coupled to the oscillators, instead, an A0-type of excitation at frequencies below $f_o = 1$ MHz generates both m_1 and m_2, since none of them exhibit purely symmetric modal displacements in the out-of-plane direction. Therefore, each plot of Fig. 4(d–f) shows the faster arrival of m_2, which has a relatively low attenuation as

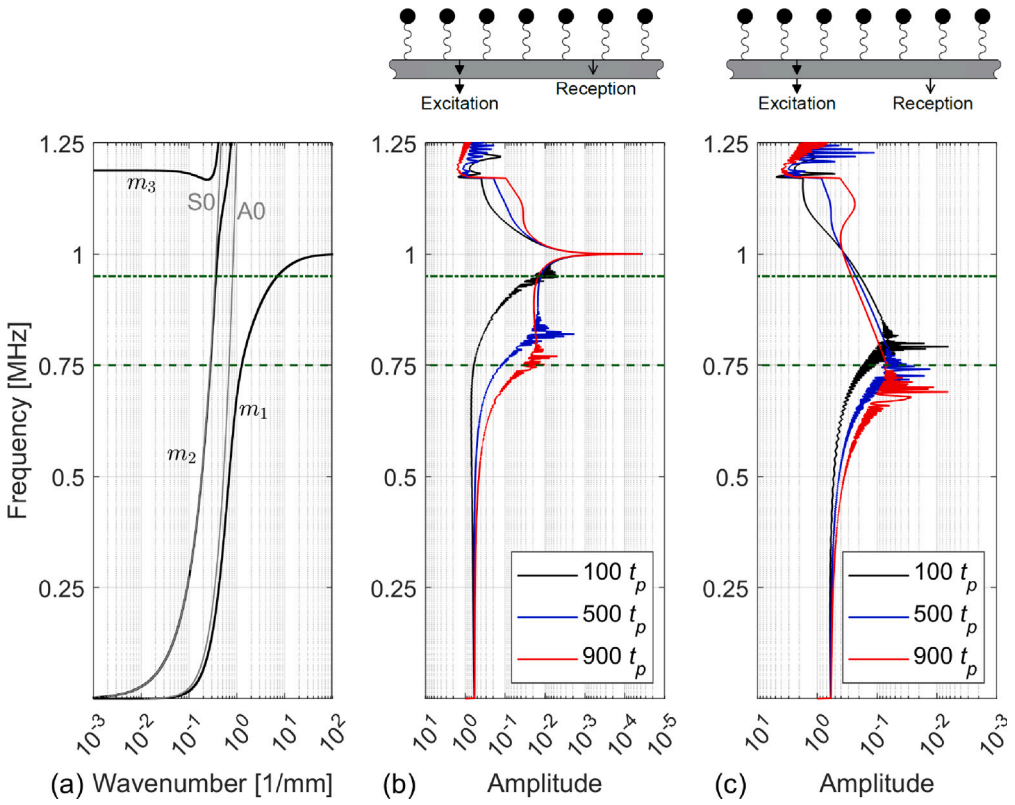

Fig. 3. 1 mm-thick steel plate in vacuum with material properties as in Table 1 and coupled to an array of oscillators with homogenized mass $m_o = 7.7$ kg/m^2, damping coefficient $c_o = 0$ and resonant frequency $f_o = 1$ MHz. (a) "Wavenumber vs. frequency" dispersion curves. (b,c) Transfer functions associated to an A0-type of excitation where receivers measure the out-of-plane displacements at (b) the top surface and (c) the bottom surface of the plate (each of these two configurations are schematized above the respective plots), and at three different propagation distances of either 100, 500 or 900 times the plate's thickness t_p (i.e., 100, 500 or 900 mm); each graph in both plots is normalized by the equivalent transfer function obtained for the traction-free plate scenario. The green dashed and dash-dotted lines indicate the center frequency of the excitation considered in Figs. 4 and 5, respectively.

seen in Fig. 2(c), and the slower arrival of m_1, which at this frequency is already very dispersive and strongly attenuated. Indeed, Fig. 4(d) reveals that the m_1's arrival after only 100 mm of propagation is already significantly dispersed, and its peak amplitude is only about a tenth of A0 in the traction-free plate at the same distance, while it is about ten times larger than that of m_2. Then, after propagating for 900 mm (Fig. 4(f)), m_1's amplitude has already dropped to the same level as m_2, and it is about an hundredth of the A0's amplitude of the traction-free plate scenario (the red arrival in Fig. 4(c)).

Similar considerations apply to Fig. 5, where the excitation pulse is centered at 0.95 MHz, i.e., much closer to f_o. Fig. 2(c) shows that at this frequency the attenuation of m_1 is much higher than at 0.75 MHz, and, indeed, already after 100 mm of propagation (Fig. 5(d)) its amplitude is less than one hundredth of the A0's amplitude in the traction-free plate scenario. At this frequency, also m_2 starts to be rather dispersive, hence its arrivals feature a dispersive tail. Note that the signals measured after 500 mm (Fig. 5(e)) and 900 mm (Fig. 5(f)) of wave propagation are essentially all due to m_2, with m_1 being attenuated to much smaller amplitudes.

3.2. Steel plate coupled to an infinite array of oscillators at its top surface and adjacent to water at the bottom

The same plate coupled to oscillators at its top surface already analyzed in the previous section is now considered adjacent to water at its bottom surface. This case study is inspired by recent research on fluid-loaded metasurfaces, originally discussed in [37] using an analytical Kirchhoff–Love plate equation.

As in previous section, the plate was discretized using 20 one-dimensional three-node elements. Water was modeled as an inviscid fluid with density $\rho_w = 1$ kg/m^3 and supporting longitudinal waves traveling at $c_w = 1500$ m/s.

This problem was implemented in Eq. (41) by setting $\rho_{f1} = 0$, $\rho_{f2} = \rho_w$, and by expressing $\mathbf{Z}(\omega)$ as in Eq. (26). The resulting generalized eigenvalue problem was then solved at a range of ω values. Note that Ward's algorithm [35] was used to balance the matrices of the problem since numerical instabilities otherwise occurred at frequencies higher than ~1.5 MHz.

Fig. 6(a–f) plot via black, red and blue traces the (a,d) "Wavenumber vs. frequency", (b,e) "Phase velocity vs. frequency" and (c,f) "Attenuation vs. frequency" dispersion curves obtained in this scenario, with plots (d–f) zooming in the green boxes of (a–c). The four black traces visible at these zoom-levels correspond to wave modes denoted m_{l1} to m_{l4}, which are the "leaky" counterparts

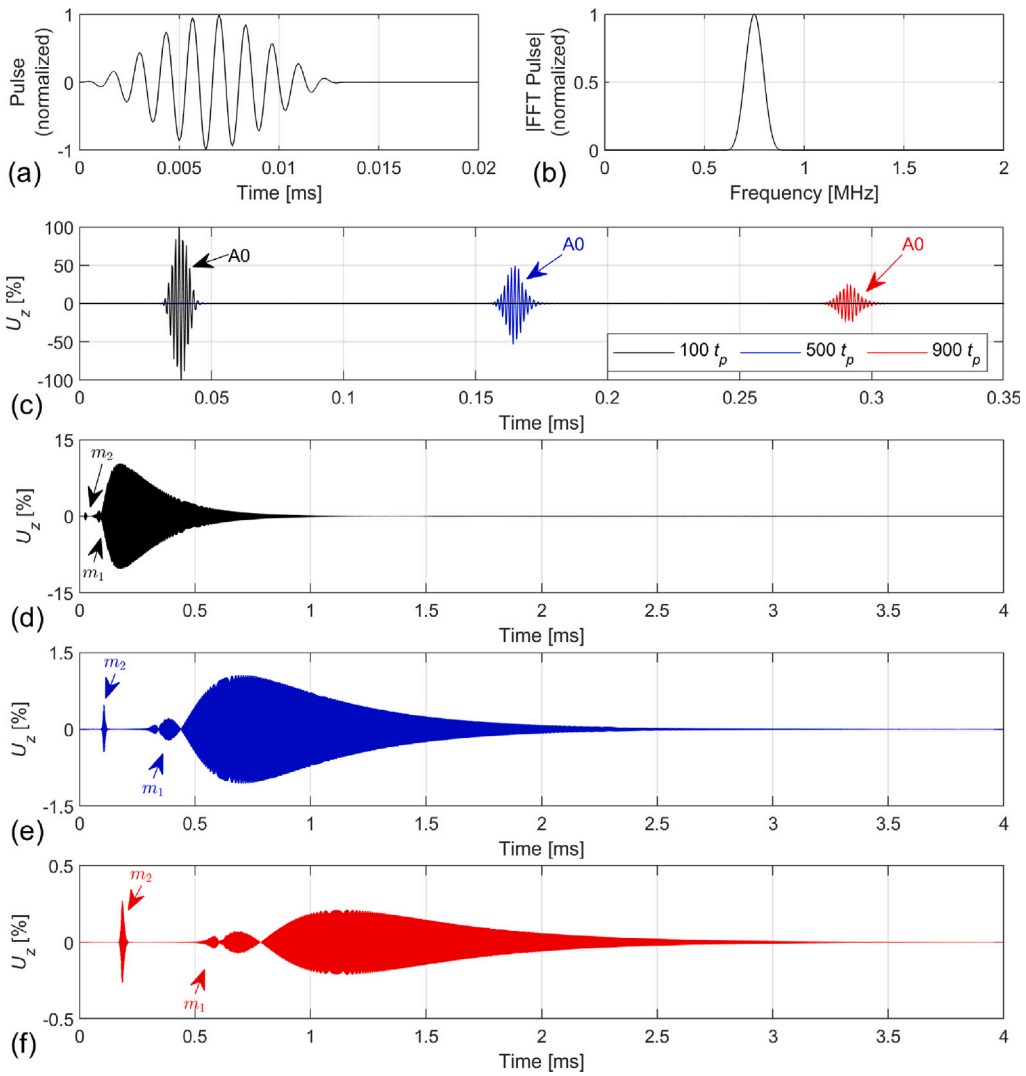

Fig. 4. Transient signals sensed by receivers measuring the out-of-plane displacement of the plate's top surface at various propagation distances from an A0-type of excitation (same transmitter/receiver configuration as Fig. 3(b)). (a–b) (a) Time–history and (b) frequency content of the excitation pulse (Hann-windowed 10 cycles centered at 0.75 MHz). (c) Case of plate without oscillators. (d–f) Case of plate coupled to oscillators, at propagation distances of 100 (d), 500 (e) and 900 (f) times the plate's thickness t_p (i.e., 100, 500 and 900 mm).

of modes m_1 to m_4 existing in the absence of water (and discussed in the previous section). The red and blue traces, instead, are two quasi-Scholte modes, denoted Sc_1 and Sc_2, which arise from the interaction between the quasi-Lamb modes in the plate and the acoustic waves in the water adjacent to the plate's bottom surface. Fig. 6(a–f) also plot via gray traces the dispersion curves obtained by solving Eq. (41) in the absence of resonators (i.e., by setting $\mathbf{Z}(\omega) = \mathbf{0}$). The quasi-Lamb modes existing in this scenario are denoted qA0, qS0 and qA1, while the quasi-Scholte mode, which overlaps with Sc_2 across the frequency range of existence of the latter one, is not labeled in figure for clarity. Finally, the three black markers in Fig. 6(d–f) indicate the modal solutions for either Sc_1 or Sc_2 whose wave shapes are plotted in Fig. 6(g–i). Note that square and circle markers are out-of-scale in plot (d).

Clearly, many of the features of Fig. 6(a–f) are similar to those of Fig. 2(a–c). Except for the existence of the quasi-Scholte modes, the most notable differences from that scenario are that m_{l3} has a short gap for wavenumbers between ~0.23 and ~0.29 1/mm (which is only visible in plot (a), as at the corresponding frequencies of ~1.16 MHz m_{l3} is extremely attenuated), and that the attenuation levels seen in Fig. 6(c) are generally higher than those of Fig. 2(c), due to leakages into water.

The zoom levels of Fig. 6(d–f) are chosen to better visualize the features of the quasi-Scholte modes. The one labeled Sc_1 is sustained by m_{l1} between the beginning of the frequency axis and $f_o = 1$ MHz, and its dispersion curves are almost overlapped with those of m_{l1} throughout most of their existence. Indeed, Fig. 6(g,h) show that Sc_1's modal displacements at 0.5 and 0.95 MHz are analogous to those of m_1 (i.e., the mode corresponding to m_{l1} in the absence of water) that are shown in Fig. 2(g,h). An interesting effect of the interaction between water and m_1/m_{l1} is that its phase velocity remains capped below $c_w = 1500$ m/s in the frequency

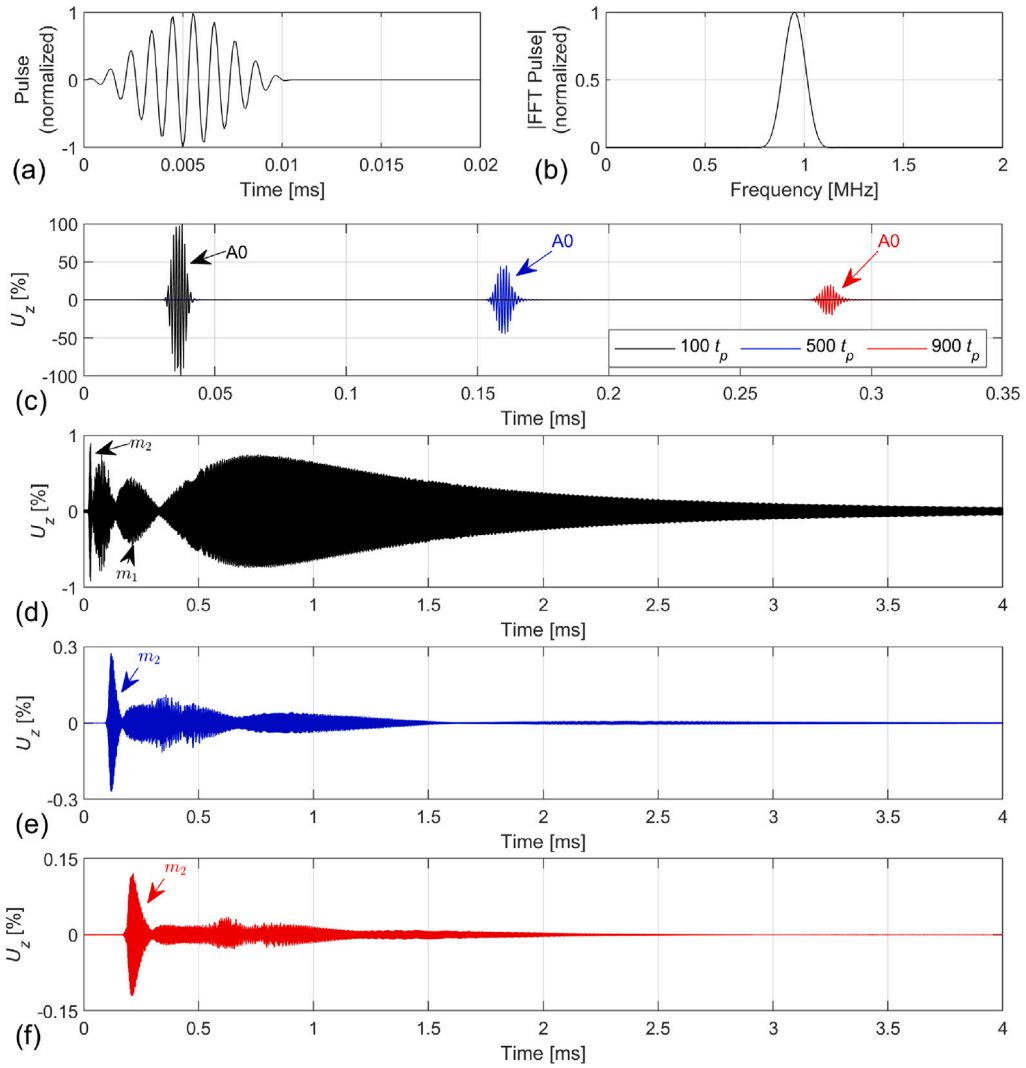

Fig. 5. Same as Fig. 4, though in here the excitation pulse is centered at 0.95 MHz.

range between ~0.4 and ~0.6 MHz, and this effect is accompanied by an increased attenuation for m_{l1} across the same frequency range. The other quasi-Scholte mode, Sc_2, originates at ~0.7 MHz, i.e., when the out-of-plane displacement at the plate's bottom surface of m_2/m_{l2} has reached a high enough amplitude that becomes capable of sustaining it. As seen in Fig. 6(c,f), Sc_2 propagates with very low attenuation, and its wave shape at 0.95 MHz is plotted in Fig. 6(i).

Also in these scenarios of fluid-coupled plates it is possible to compute frequency and time-transient responses due to a desired forcing source, as similarly done in Section 3.1.1. This can be accomplished by applying the procedure proposed in [38] to the SAFE formulation presented in Section 2.2. As a matter of example, Fig. 7(a) re-plots the "Wavenumber vs. frequency" dispersion curves of Fig. 6(a) in a semi-logarithmic scale, while Fig. 7(b,c) show via solid lines the transfer functions associated to an A0-type of excitation for receivers measuring the out-of-plane displacements at either (b) the top or (c) the bottom surface of the same plate studied above, at a propagation distance of 10 times the plate's thickness (i.e., 10 mm). Note that a much smaller propagation distance was chosen in here with respect to those considered in Fig. 3, since in this scenario the propagating waves are subjected to a much increased attenuation due to the coupling with water. For comparison purposes, the figure also shows in dashed line the equivalent plot obtained in the absence of water (i.e., the same scenario as in Fig. 3). As in Fig. 3(b,c), each graph in Fig. 7 was obtained by normalizing each transfer function by the equivalent function obtained in the absence of oscillators. Similarly as for the plate in vacuum, also in the water-coupled scenario the out-of-plane motion at the plate's top surface (Fig. 7(b)) has a significant dip at 1 MHz (the oscillators' resonant frequency), while that at the plate's bottom surface does not exhibit this feature (Fig. 7(c)). Also, the solid line of Fig. 7(b) shows that in the water-coupled scenario after 10 mm of wave propagation there is already a rather wide frequency-band below $f_o = 1$ MHz at very low amplitude. Furthermore, both plots (b,c) show that the resonators in the water-coupled plate cause frequency-dependent changes to the transfer functions also at frequencies much smaller than the

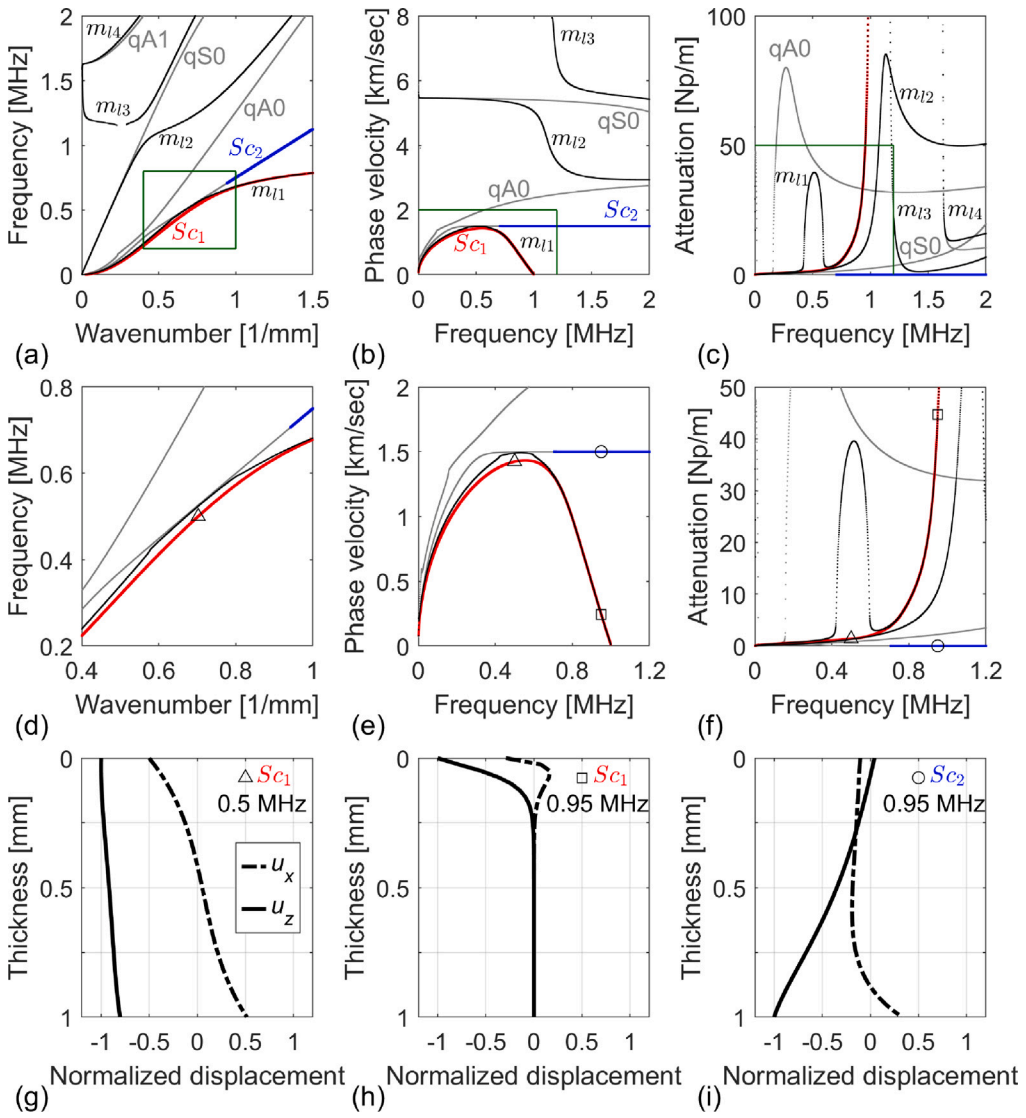

Fig. 6. 1 mm-thick steel plate with material properties as in Table 1, coupled at its upper surface to an array of oscillators with homogenized mass $m_o = 7.7$ kg/m^2, damping coefficient $c_o = 0$ and resonant frequency $f_o = 1$ MHz and at its lower surface to water (modeled with $\rho_w = 1$ kg/m^3 and $c_w = 1500$ m/s). (a,d) "Wavenumber vs. frequency", (b,e) "Phase velocity vs. frequency" and (c,f) "Attenuation vs. frequency" dispersion curves (black lines for quasi-Lamb; red and blue lines for quasi-Scholte), compared to those obtained in the absence of resonators (gray lines); (d–f) zoom in the green boxes shown in (a–c); the three black markers in plots (d–f) pinpoint the solutions for which the corresponding modal shapes are plotted in (g–i) (square and circle markers are out-of-scale in plot (d)). (g–i) Cross-sectional displacement wave shapes.

resonant one (say, below 0.75 MHz). This more complicated behavior has partly to do with the different and frequency-varying levels of attenuation seen in Fig. 7(c) for the two pairs of modes qA0/quasi-Scholte and m_{l1}/Sc_1 in the two scenarios of absence or presence of water, respectively, and partly with the different and frequency-dependent degrees of excitability of these two pairs of modes when the plate is subjected to an A0-type of excitation. Features as these ones are rather difficult to predict via the sole analysis of dispersion curves and modal shapes, and hence this is a very good example to show the potential benefit of plotting transfer function curves.

4. Conclusions

A semi-analytical finite element formulation that aids the analysis of waves propagating in plates coupled to metasurfaces has been presented. The framework enables the modeling of any metasurface whose action can be expressed in terms of the tractions it exerts on the plate's surface. Any layered plate whose materials have linear viscoelastic constitutive relations which can be formulated in the frequency domain can be considered. Furthermore, the plate can be either in vacuum or coupled to an inviscid

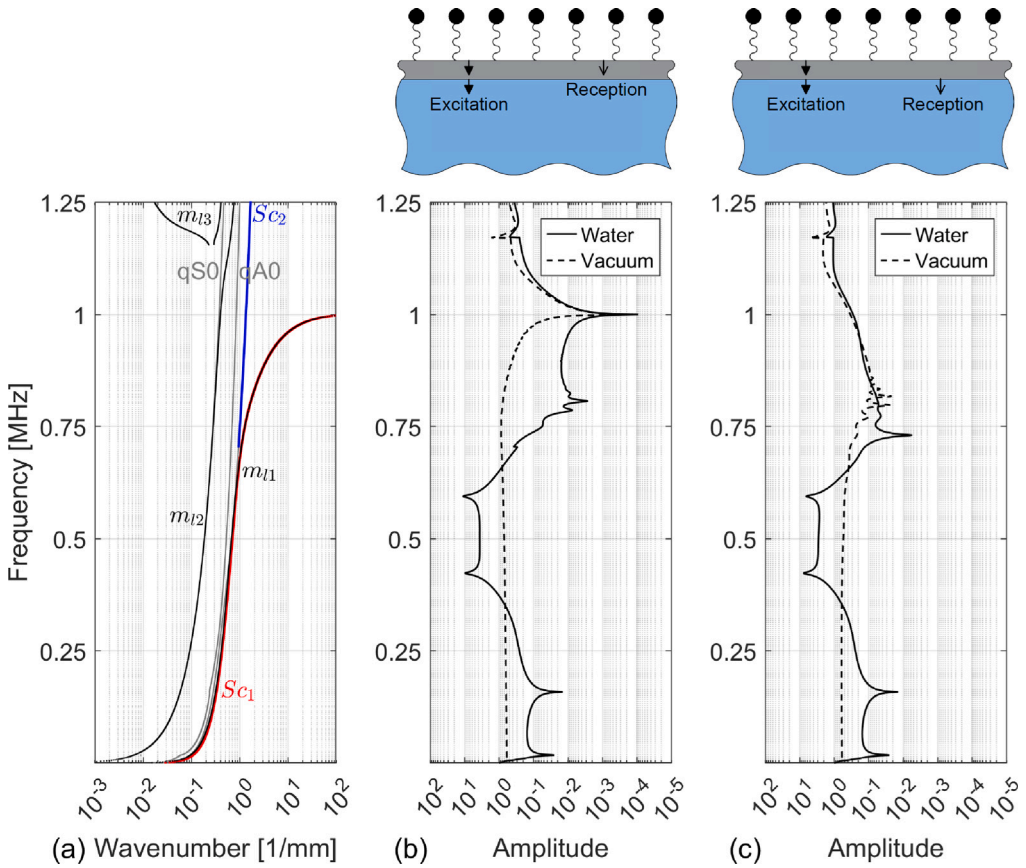

Fig. 7. (a) "Wavenumber vs. frequency" dispersion curves for a 1 mm-thick steel plate with material properties as in Table 1, coupled at its upper surface to an array of oscillators with homogenized mass $m_o = 7.7$ kg/m^2, damping coefficient $c_o = 0$ and resonant frequency $f_o = 1$ MHz and at its lower surface to water (modeled with $\rho_w = 1$ kg/m^3 and $c_w = 1500$ m/s). (b,c) Transfer functions associated to an A0-type of excitation where receivers measure the out-of-plane displacements at (b) the top surface and (c) the bottom surface of the plate (each of these two configurations are schematized above the respective plots) at a propagation distance of 10 times the plate's thickness (10 mm); the solid lines refer to the scenario of (a), i.e., plate adjacent to water, while the dashed lines refer to the plate in vacuum, i.e., same scenario as in Fig. 3. Each graph in both plots is normalized by the equivalent transfer function obtained in the absence of oscillators.

fluid, in which case quasi-Scholte modes are also derived. The formulation enables the computation of dispersion curves, cross-sectional wave shapes, transfer functions and transient signals propagating within the structure in response to any desired forcing excitation. Depending on the geometry of the problem and the parameters chosen for the analysis, each calculation should only take up to a few minutes on any low- to mid-level CPU. Finally, the presented scheme has the potential to be further generalized to deal with plates formed by multi-layered anisotropic materials, even when they are coupled to isotropic elastic half-spaces [39], or with waveguides of arbitrary cross-sections [10].

The numerical examples presented in the article focused on a viscoelastic steel plate, either in vacuum or in water, coupled to an infinite array of mass–spring–dashpot oscillators. The resulting dispersion curves and cross-sectional wave shapes were discussed. For both in-vacuum and in-water scenarios, it was shown that a mode that at low frequencies behaves as A0 (or quasi-A0 for the plate in water) tends to a null phase velocity and to an extremely high attenuation towards the resonant frequency of the resonators, while another mode that at low frequencies behaves as S0 (or quasi-S0) can pass through such frequency value by modifying its modal shape so that no out-of-plane displacements occur at the surface where plate and resonators are coupled. At a frequency higher than resonance, a third mode appears, whose wave shape near its cut-on frequency loosely resembles that of A0 (or quasi-A0). Then, at higher frequencies, its dispersion relations tend towards those of S0 (or quasi-S0). Furthermore, for the in-water configuration, it was shown that the modes discussed above support two quasi-Scholte waves, one of which ceases to exist at the oscillators' resonance, while the other appears at a frequency lower than resonance. Finally, some examples of transfer functions and transient signals were given and discussed in order to illustrate the potential of the proposed formulation for studying wave propagation in waveguides of finite length.

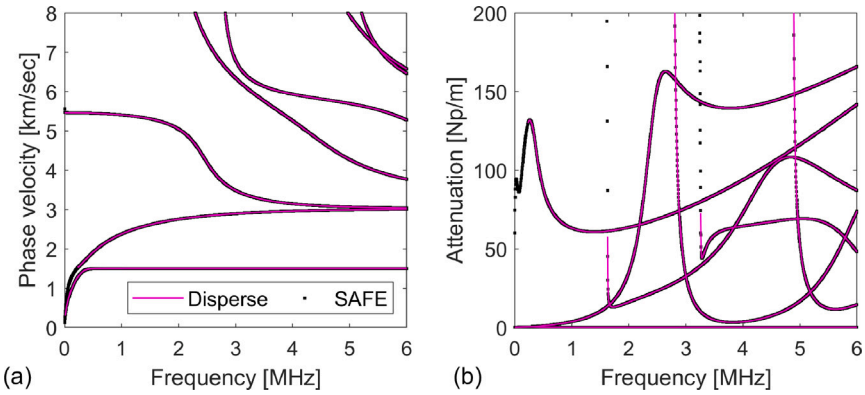

Fig. B.1. (a) "Phase velocity vs. frequency" and (b) "Attenuation vs. frequency" dispersion curves for a 1 mm-thick steel plate with material properties as in Table 1 and immersed in water having density of 1 kg/m^3 and supporting longitudinal waves traveling at 1500 m/s. Black dots and magenta lines plot the solutions given by the SAFE implementation of Section 2.2 and by Disperse [5], respectively.

CRediT authorship contribution statement

S. Mariani: Writing – original draft, Visualization, Validation, Software, Project administration, Methodology, Investigation, Formal analysis, Data curation, Conceptualization. **A. Palermo:** Writing – review & editing, Validation, Software, Methodology, Investigation, Formal analysis, Conceptualization. **A. Marzani:** Writing – review & editing, Validation, Software, Methodology, Investigation, Formal analysis, Conceptualization.

Declaration of competing interest

The authors declare that they have no known competing financial interests or personal relationships that could have appeared to influence the work reported in this paper.

Acknowledgments

The first author is grateful to the "Programma per Giovani Ricercatori Rita Levi Montalcini year 2020" (grant PGR20WNZMY) of the Italian Ministry of University and Research (MUR) for the financial support.

Appendix A. Wave finite element model

The WFE model implemented in COMSOL Multiphysics consists of a 3D portion of a 1 mm-thick steel plate having material properties as in Table 1. The plate's portion is a cuboid with sides of 0.001 mm in the planar extension and with the full plate's thickness of 1 mm. This volume was discretized via tetrahedral elements, with the mesh being refined until convergence. A resonator was modeled as a truss element oriented in a perpendicular direction with respect to the plate's plane, whose lower end was linked to the upper surface of the plate and with a point mass assigned to its upper end. Such truss element was modeled as a COMSOL's "spring-damper" object, which effectively models a mass–spring–dashpot oscillator. The values assigned to the point mass and the stiffness of the spring are those obtained by multiplying the homogenized oscillator properties considered in Section 3 by the planar area of the modeled portion of the plate, i.e., by 0.001×0.001 mm^2. Floquet periodic boundary conditions were applied at the four outer cross-sectional faces of the portioned plate in order to model infinite planar extension [6]. The eigenfrequency problem for this model was solved by setting real wavenumbers at steps of ~161 1/m, and by thus obtaining a number of associated complex eigenfrequencies, the real parts of which are plotted as red markers in Fig. 2(a).

Appendix B. Steel plate immersed in water without resonators

A 1 mm-thick steel plate with the same material properties as that studied in Section 3 (Table 1) is considered in here, though in this case the plate is modeled as completely immersed in water (i.e., water is adjacent to both lower and upper surfaces of the plate) and it is not loaded by resonators. As in Section 3, the plate was discretized using 20 one-dimensional three-node elements. Water was modeled using the same properties used in Section 3.2 (i.e., $\rho_w = 1$ kg/m^3 and $c_w = 1500$ m/s). The generalized eigenvalue problem of Eq. (41), with both ρ_{f1} and ρ_{f2} set equal to ρ_w, and with $\mathbf{Z}(\omega)$ set to zero, was solved at a range of ω values. Ward's balancing algorithm was used in order to avoid numerical instabilities [35].

This problem was also setup in Disperse [5] in order to verify the results given by the SAFE algorithm of Section 2.2. Fig. B.1 shows the (a) "Phase velocity vs. frequency" and (b) "Attenuation vs. frequency" dispersion curves given by SAFE using black dots, while those of Disperse [5] are displayed via magenta lines. An excellent agreement is observed, thus confirming the validity of the SAFE implementation described in Section 2.2.

Data availability

Data will be made available on request.

References

[1] P. Cawley, Guided waves in long range nondestructive testing and structural health monitoring: Principles, history of applications and prospects, NDT E Int. (2023) 103026, http://dx.doi.org/10.1016/j.ndteint.2023.103026.
[2] X. Zang, Z.-D. Xu, H. Lu, C. Zhu, Z. Zhang, Ultrasonic guided wave techniques and applications in pipeline defect detection: A review, Int. J. Press. Vessels Pip. (2023) 105033, http://dx.doi.org/10.1016/j.ijpvp.2023.105033.
[3] J. Rose, Ultrasonic Guided Waves in Solid Media, Cambridge University Press, 2014.
[4] L. Knopoff, A matrix method for elastic wave problems, Bull. Seismol. Soc. Am. 54 (1) (1964) 431–438, http://dx.doi.org/10.1785/BSSA0540010431.
[5] B. Pavlakovic, M. Lowe, D. Alleyne, P. Cawley, Disperse: A general purpose program for creating dispersion curves, in: Review of Progress in Quantitative Nondestructive Evaluation: Volume 16A, Springer, 1997, pp. 185–192.
[6] B.R. Mace, E. Manconi, Modelling wave propagation in two-dimensional structures using finite element analysis, J. Sound Vib. 318 (4–5) (2008) 884–902, http://dx.doi.org/10.1016/j.jsv.2008.04.039.
[7] T. Hoang, D. Duhamel, G. Foret, Wave finite element method for waveguides and periodic structures subjected to arbitrary loads, Finite Elem. Anal. Des. 179 (2020) 103437, http://dx.doi.org/10.1016/j.finel.2020.103437.
[8] L. Gavrić, Computation of propagative waves in free rail using a finite element technique, J. Sound Vib. 185 (3) (1995) 531–543, http://dx.doi.org/10.1006/jsvi.1995.0398.
[9] T. Hayashi, W.-J. Song, J.L. Rose, Guided wave dispersion curves for a bar with an arbitrary cross-section, a rod and rail example, Ultrasonics 41 (3) (2003) 175–183, http://dx.doi.org/10.1016/S0041-624X(03)00097-0.
[10] I. Bartoli, A. Marzani, F.L. Di Scalea, E. Viola, Modeling wave propagation in damped waveguides of arbitrary cross-section, J. Sound Vib. 295 (3–5) (2006) 685–707, http://dx.doi.org/10.1016/j.jsv.2006.01.021.
[11] D.A. Kiefer, M. Ponschab, S.J. Rupitsch, M. Mayle, Calculating the full leaky lamb wave spectrum with exact fluid interaction, J. Acoust. Soc. Am. 145 (6) (2019) 3341–3350, http://dx.doi.org/10.1121/1.5109399.
[12] Y. Pennec, B. Djafari-Rouhani, H. Larabi, J.O. Vasseur, A. Hladky-Hennion, Low-frequency gaps in a phononic crystal constituted of cylindrical dots deposited on a thin homogeneous plate, Phys. Rev. B— Condens. Matter Mater. Phys. 78 (10) (2008) 104105, http://dx.doi.org/10.1103/PhysRevB.78.104105.
[13] T.-T. Wu, Z.-G. Huang, T.-C. Tsai, T.-C. Wu, Evidence of complete band gap and resonances in a plate with periodic stubbed surface, Appl. Phys. Lett. 93 (11) (2008) http://dx.doi.org/10.1063/1.2970992.
[14] H.-b. Zhang, J.-j. Chen, X. Han, Lamb wave band gaps in a homogenous plate with periodic tapered surface, J. Appl. Phys. 112 (5) (2012) http://dx.doi.org/10.1063/1.4749400.
[15] Y. Li, L. Zhu, T. Chen, Plate-type elastic metamaterials for low-frequency broadband elastic wave attenuation, Ultrasonics 73 (2017) 34–42, http://dx.doi.org/10.1016/j.ultras.2016.08.019.
[16] A. Khelif, Y. Achaoui, B. Aoubiza, In-plane confinement and waveguiding of surface acoustic waves through line defects in pillars-based phononic crystal, AIP Adv. 1 (4) (2011) http://dx.doi.org/10.1063/1.3675923.
[17] A. Colombi, R.V. Craster, D. Colquitt, Y. Achaoui, S. Guenneau, P. Roux, M. Rupin, Elastic wave control beyond band-gaps: Shaping the flow of waves in plates and half-spaces with subwavelength resonant rods, Front. Mech. Eng. 3 (2017) 10, http://dx.doi.org/10.3389/fmech.2017.00010.
[18] Y. Jin, W. Wang, A. Khelif, B. Djafari-Rouhani, Elastic metasurfaces for deep and robust subwavelength focusing and imaging, Phys. Rev. Appl. 15 (2) (2021) 024005, http://dx.doi.org/10.1103/PhysRevApplied.15.024005.
[19] D. Colquitt, A. Colombi, R. Craster, P. Roux, S. Guenneau, Seismic metasurfaces: Sub-wavelength resonators and Rayleigh wave interaction, J. Mech. Phys. Solids 99 (2017) 379–393, http://dx.doi.org/10.1016/j.jmps.2016.12.004.
[20] G. Carta, D. Colquitt, A. Movchan, N. Movchan, I. Jones, Chiral flexural waves in structured plates: Directional localisation and control, J. Mech. Phys. Solids 137 (2020) 103866, http://dx.doi.org/10.1016/j.jmps.2020.103866.
[21] X. Pu, A. Marzani, A. Palermo, A multiple scattering formulation for elastic wave propagation in space–time modulated metamaterials, J. Sound Vib. 573 (2024) 118199, http://dx.doi.org/10.1016/j.jsv.2023.118199.
[22] M. Martí-Sabaté, D. Torrent, Edge modes for flexural waves in quasi-periodic linear arrays of scatterers, APL Mater. 9 (8) (2021) http://dx.doi.org/10.1063/5.0059097.
[23] P. Packo, A.N. Norris, D. Torrent, Metaclusters for the full control of mechanical waves, Phys. Rev. Appl. 15 (1) (2021) 014051, http://dx.doi.org/10.1103/PhysRevApplied.15.014051.
[24] A.B. Movchan, R.C. McPhedran, G. Carta, Scattering reduction and resonant trapping of flexural waves: Two rings to rule them, Appl. Sci. 11 (10) (2021) 4462, http://dx.doi.org/10.3390/app11104462.
[25] Y. Jin, Y. Pennec, B. Bonello, H. Honarvar, L. Dobrzynski, B. Djafari-Rouhani, M.I. Hussein, Physics of surface vibrational resonances: Pillared phononic crystals, metamaterials, and metasurfaces, Rep. Progr. Phys. 84 (8) (2021) 086502, http://dx.doi.org/10.1088/1361-6633/abdab8.
[26] J. Sánchez-Dehesa, A. Krokhin, Introduction to acoustics of phononic crystals. Homogenization at low frequencies, in: Phononic Crystals: Fundamentals and Applications, Springer, 2016, pp. 1–21.
[27] D. Torrent, J. Sánchez-Dehesa, Multiple scattering formulation of two-dimensional acoustic and electromagnetic metamaterials, New J. Phys. 13 (9) (2011) 093018, http://dx.doi.org/10.1088/1367-2630/13/9/093018.
[28] E. Miranda Jr., S. Rodrigues, C. Aranas Jr., J. Dos Santos, Plane wave expansion and extended plane wave expansion formulations for mindlin-Reissner elastic metamaterial thick plates, J. Math. Anal. Appl. 505 (2) (2022) 125503, http://dx.doi.org/10.1016/j.jmaa.2021.125503.
[29] D. Krattiger, M.I. Hussein, Bloch mode synthesis: Ultrafast methodology for elastic band-structure calculations, Phys. Rev. E 90 (6) (2014) 063306, http://dx.doi.org/10.1103/PhysRevE.90.063306.
[30] A. Marzani, Time–transient response for ultrasonic guided waves propagating in damped cylinders, Int. J. Solids Struct. 45 (25–26) (2008) 6347–6368, http://dx.doi.org/10.1016/j.ijsolstr.2008.07.028.
[31] T. Hayashi, D. Inoue, Calculation of leaky lamb waves with a semi-analytical finite element method, Ultrasonics 54 (6) (2014) 1460–1469, http://dx.doi.org/10.1016/j.ultras.2014.04.021.
[32] A. Maznev, V. Gusev, Waveguiding by a locally resonant metasurface, Phys. Rev. B 92 (11) (2015) 115422, http://dx.doi.org/10.1103/PhysRevB.92.115422.
[33] H. Gravenkamp, C. Birk, C. Song, Numerical modeling of elastic waveguides coupled to infinite fluid media using exact boundary conditions, Comput. Struct. 141 (2014) 36–45, http://dx.doi.org/10.1016/j.compstruc.2014.05.010.
[34] M.C. Junger, D. Feit, Sound, structures, and their interaction, vol. 225, MIT press Cambridge, MA, 1986.
[35] R.C. Ward, Balancing the generalized eigenvalue problem, SIAM J. Sci. Stat. Comput. 2 (2) (1981) 141–152, http://dx.doi.org/10.1137/0902012.
[36] O.M. Mukdadi, S.K. Datta, Transient ultrasonic guided waves in layered plates with rectangular cross section, J. Appl. Phys. 93 (11) (2003) 9360–9370, http://dx.doi.org/10.1063/1.1573734.

[37] E. Skelton, R. Craster, A. Colombi, D. Colquitt, The multi-physics metawedge: Graded arrays on fluid-loaded elastic plates and the mechanical analogues of rainbow trapping and mode conversion, New J. Phys. 20 (5) (2018) 053017, http://dx.doi.org/10.1088/1367-2630/aabecf.

[38] D. Inoue, T. Hayashi, Transient analysis of leaky lamb waves with a semi-analytical finite element method, Ultrasonics 62 (2015) 80–88, http://dx.doi.org/10.1016/j.ultras.2015.05.004.

[39] H. Gravenkamp, B. Plestenjak, D.A. Kiefer, E. Jarlebring, Computation of leaky waves in layered structures coupled to unbounded media by exploiting multiparameter eigenvalue problems, J. Sound Vib. 596 (2025) 118716, http://dx.doi.org/10.1016/j.jsv.2024.118716.